Cancer Research

AACR

A New Three-Dimensional Ultrasound Microimaging Technology for Preclinical Studies Using a Transgenic Prostate Cancer Mouse Model

Lauren A. Wirtzfeld, Guojun Wu, Michael Bygrave, et al.

Updated version	Access the most recent version of this article at: http://cancerres.aacrjournals.org/content/65/14/6337
Supplementary Material	Access the most recent supplemental material at: http://cancerres.aacrjournals.org/content/suppl/2005/07/14/65.14.6337.DC1.html

Cited Articles	This article cites by 20 articles, 7 of which you can access for free at: http://cancerres.aacrjournals.org/content/65/14/6337.full.html#ref-list-1
Citing articles	This article has been cited by 18 HighWire-hosted articles. Access the articles at: http://cancerres.aacrjournals.org/content/65/14/6337.full.html#related-urls

E-mail alerts	Sign up to receive free email-alerts related to this article or journal.
Reprints and Subscriptions	To order reprints of this article or to subscribe to the journal, contact the AACR Publications Department at pubs@aacr.org.
Permissions	To request permission to re-use all or part of this article, contact the AACR Publications Department at permissions@aacr.org.

A New Three-Dimensional Ultrasound Microimaging Technology for Preclinical Studies Using a Transgenic Prostate Cancer Mouse Model

Lauren A. Wirtzfeld,[1,7] Guojun Wu,[2] Michael Bygrave,[7] Yasuto Yamasaki,[2,8] Hideki Sakai,[8] Madeleine Moussa,[3] Jonathan I. Izawa,[2] Dónal B. Downey,[4,7] Norman M. Greenberg,[9] Aaron Fenster,[4,5,7] Jim W. Xuan,[2,3] and James C. Lacefield[5,6,7]

[1]Biomedical Engineering Graduate Program and Departments of [2]Surgery, [3]Pathology, [4]Diagnostic Radiology and Nuclear Medicine, [5]Medical Biophysics, and [6]Electrical and Computer Engineering, University of Western Ontario; [7]Imaging Research Laboratories, Robarts Research Institute, London, Ontario, Canada; [8]Department of Urology, Nagasaki University School of Medicine, Nagasaki, Japan; and [9]Clinical Research Division, Fred Hutchinson Cancer Research Center, Seattle, Washington

Abstract

Prostate cancer is the most common cancer in adult men in North America. Preclinical studies of prostate cancer employ genetically engineered mouse models, because prostate cancer does not occur naturally in rodents. Widespread application of these models has been limited because autopsy was the only reliable method to evaluate treatment efficacy in longitudinal studies. This article reports the first use of three-dimensional ultrasound microimaging for measuring tumor progression in a genetically engineered mouse model, the 94–amino acid prostate secretory protein gene-directed transgenic prostate cancer model. Qualitative comparisons of three-dimensional ultrasound images with serial histology sections of prostate tumors show the ability of ultrasound to accurately depict the size and shape of malignant masses in live mice. Ultrasound imaging identified tumors ranging from 2.4 to 14 mm maximum diameter. The correlation coefficient of tumor diameter measurements done *in vivo* with three-dimensional ultrasound and at autopsy was 0.998. Prospective tumor detection sensitivity and specificity were both >90% when diagnoses were based on repeated ultrasound examinations done on separate days. Representative exponential growth curves constructed via longitudinal ultrasound imaging indicated volume doubling times of 5 and 13 days for two prostate tumors. Compared with other microimaging and molecular imaging modalities, the application of three-dimensional ultrasound imaging to prostate cancer in mice showed advantages, such as high spatial resolution and contrast in soft tissue, fast and uncomplicated protocols, and portable and economical equipment that will likely enable ultrasound to become a new microimaging modality for mouse preclinical trial studies. (Cancer Res 2005; 65(14): 6337-45)

Introduction

Prostate cancer is the most common cancer in adult men in North America. Because there is no naturally occurring prostate cancer in small animals, preclinical studies employ genetically engineered mouse models. Several mouse prostate cancer models with features similar to the human disease, such as the rat probasin gene-based transgenic adenocarcinoma of the prostate (TRAMP; ref. 1) and LPB-SV40 tag (2) models, have been produced using transgenic and knockout techniques (for reviews, see refs. 3, 4). However, the stochastic and often invisible nature of genetically engineered murine prostate tumor models has thus far limited their widespread application. In contrast to the number of markers developed for human prostate cancer, no protein counterpart to prostate-specific antigen (PSA) has been identified in rodents, and few serum tumor markers exist for murine prostate cancer. Preclinical trials require large treatment cohorts of mice to generate statistically meaningful data, and autopsy is often the most effective way to evaluate treatment efficacy, so longitudinal studies examining the dynamics of tumor response and relapse after treatment are cumbersome when conventional laboratory methods are used. These challenges complicate attempts to synchronize treatment with the development of tumor burden because conventional tumor latency-based estimates are prone to a high degree of error.

In clinical oncology, measurements of changes in tumor size obtained from diagnostic images are a standard method of monitoring patient response to anticancer therapies (5). The recent development of high-resolution microimaging technologies for use with small laboratory animals has made equivalent measurements possible in mouse cancer models (6). Longitudinal measurements of changes in tumor size in a transgenic prostate cancer model were first done using two-dimensional magnetic resonance imaging (MRI; ref. 7). The development of prostate-specific promoters has also made *in vivo* monitoring of transgenic expression possible using bioluminescence imaging of luciferase reporter genes. This technique was first shown by manipulation of human PSA promoter-directed luciferase in a recombinant adenovirus in a xenograft-based model (8). An improved approach employs adenovirus-mediated delivery of cre− recombination in normal transgenic mice (9). A human *hk2* gene promoter-directed EZC-prostate model has also been established for longitudinal monitoring (10).

Noninvasive tumor monitoring was also among the first applications identified for ultrasound microimaging (11). Three-dimensional imaging capabilities could significantly improve the accuracy and efficiency of tumor volume measurements obtained

from ultrasound microimaging (11). This article reports the first use of three-dimensional ultrasound microimaging for measuring tumor progression in a genetically engineered mouse model, the transgenic mouse adenocarcinoma of the prostate (TGMAP) directed by the 94–amino acid prostate secretory protein (*PSP94*) gene promoter/enhancer region (12–14). The PSP94-TGMAP model showed similarities to the most commonly used transgenic mouse prostate cancer model, the TRAMP model (1, 12). These features include spatial (prostate tissue) and temporal (after puberty) specificity of tumor induction, fast tumor growth, similar histopathologic grading, androgen dependence, and responsive and refractory to castration deprivation therapy (12–14). The following sections present cross-sectional and longitudinal imaging studies that show the sensitivity and specificity of three-dimensional ultrasound for detecting prostate tumors in mice when the tumors are too small to be palpable and illustrate the use of ultrasound imaging to measure the rapid growth of murine prostate tumors *in situ*. Qualitative comparisons of ultrasound images with H&E-stained pathology slides are also presented that suggest some histologic features of primary and metastatic tumors in the PSP94 model that may contribute to tumor identification in ultrasound images.

Materials and Methods

Microscopic and Macroscopic Prostate Cancer in Genetically Engineered Transgenic Mice, Dissection, and Histology and Pathology Analysis

In a previous study, we used a 3.84-kb promoter/enhancer region of the *PSP94* gene directing SV40 T/t antigen targeted specifically to mouse prostate tissue [strain F1 (C57BL/6 × CBA)] to establish a model of PSP-TGMAP (*PSP94* gene-directed transgenic mouse of adenocarcinoma in the prostate; refs. 12–14). Similar to the TRAMP model, most of PSP94 transgenic mice develop fast-growing tumors in lobes of the ventral prostate, dorsolateral prostate, and anterior prostate (the coagulation gland) within 4 to 8 months of age. Transgenic mice were identified by a quick PCR genotyping protocol (12–14). All animal experiments were conducted according to standard protocols approved by the University of Western Ontario Council on Animal Care (London, Ontario, Canada).

After imaging, mice with tumors were euthanized. A dissection procedure was followed as per refs. 12–14. In brief, the prostate tissue, including ventral prostate, dorsolateral prostate, and anterior prostate, the male accessory gland (seminal vesicles), and the whole bladder were removed for gross examination and serial sectioning. Histopathologic characterization and standard definitions of various degrees of mouse prostatic intraepithelial neoplasia, as well as well, moderately, and poorly differentiated prostate cancers, were classified as we reported previously (12–14).

The terms "microscopic" and "macroscopic" cancer were employed in this study to distinguish between tumors of sizes that could be expected to be detectable with three-dimensional ultrasound in comparison with cancer on scales relevant to histology and pathology. In this study, macroscopic tumors mean prostate cancer larger than 1 mm in diameter. As reported previously (12–14), PSP-TGMAP mice classified as negative by ultrasound still possess microscopic foci of various degrees of mouse prostate cancer that have not formed large, fast-growing masses.

Three-dimensional Reconstruction of Serial H&E-stained Histology Slides

Mouse prostate tissue along with male accessory glands and bladder tissues were fixed, embedded in paraffin, sliced into 5 μm thick slides, and H&E stained. Every 10th slide (i.e., slides at 50 μm spacing) was digitized at ×10 magnification using a video microscopy system. Approximately 900 images were needed to completely digitize each slide at this magnification, and each set of 900 images was combined to obtain a single composite two-

dimensional image of a slide. Three-dimensional digitized histology volumes were constructed by aligning each composite two-dimensional image with the composite image of the slide obtained from 50 μm below. Coarse alignment was done manually by visually comparing features in neighboring slides; then, fine alignment was completed by numerical correlation of color pixels in neighboring slides.

Three-dimensional Ultrasound Image Acquisition

Mice were anesthetized with 2% isofluorane in oxygen and restrained on a heated stage (THM-100, Indus Instruments, Houston, TX) during imaging. The abdomen was depilated with a calcium thioglycolate–based consumer hair removal cream to prevent air trapped in the fur from interfering with ultrasound coupling into the animal. Ultrasound coupling gel (Aquasonic 100, Parker Laboratories, Inc., Fairfield, NJ) was applied to the depilated skin, and images of the prostate and neighboring anatomy were acquired through the ventral body wall in transverse and sagittal orientations.

Ultrasound imaging was done using a microimaging system (Vevo 660, VisualSonics, Inc., Toronto, Ontario, Canada) similar in design to the instrument described by Foster et al. (15) that employs a three-dimensional image acquisition method and three-dimensional image reconstruction and visualization software developed by our laboratory (16). The system uses a single-element, 30 MHz center frequency probe that produces a $55 \times 115 \times 115 \ \mu m^3$ resolution volume at the 12.7 mm focal depth. Images were acquired with the region of interest centered at the focus. In the three-dimensional acquisition method (16), a motorized drive mechanism linearly translates the ultrasound probe across the mouse's skin, as two-dimensional images are acquired at regular spatial intervals so they are parallel and uniformly spaced at 30 μm intervals over a $12 \times 12 \times 9 \ mm^3$ volume. The predefined parallel geometry of the two-dimensional image planes enables fast three-dimensional image reconstruction and display immediately after a scan. Three-dimensional image acquisition and reconstruction requires ∼30 seconds.

The reconstructed three-dimensional image is displayed in a dynamic cube view format (16) as a polyhedron with the appropriate image painted on each face. The user can rotate the polyhedron to any orientation and any of the faces can be moved in or out (i.e., sliced) or reoriented obliquely while the ultrasound data displayed on the face are updated in real time. In this way, the appearance of a solid polyhedron provides the user with three-dimensional cues relating the plane being manipulated to the other planes in the image volume. The three-dimensional reconstruction and analysis software has been licensed to VisualSonics for distribution with the microimaging system. Stand-alone copies of the software are available for research purposes by contacting one of the authors (J.C.L.).

Tumors were identified prospectively in the three-dimensional ultrasound images by consensus of the ultrasound system operators (L.A.W., G.W., and M.B.) and a radiologist experienced in human prostate ultrasound imaging (D.B.D.). The observers had access to all previously acquired images, and their interpretations were made with knowledge of prior imaging observations for each mouse. The accuracy of each diagnosis was determined based on the presence or absence of macroscopic tumors that were identified at autopsy and confirmed to be cancerous by histopathology. These data were used to compute tumor detection sensitivities and specificities for the ultrasound technique.

Ultrasound and histology correlation was achieved by slicing through a three-dimensional ultrasound image in a variety of different orientations to search for ultrasound views that matched the planes of the histology slices. Corresponding planes were identified by visually comparing the shape of the prostate and the appearance of regions of the most poorly differentiated, high-grade tumor in the ultrasound and histology images and by using the points where the seminal vesicles joined the prostate as anatomic landmarks for aligning the two sets of images.

Tumor Diameter, Volume, and Growth Curve Measurements

Maximum sagittal diameters of macroscopic tumors were measured using a ruler and compared with diameters measured using the three-dimensional ultrasound image analysis software. The distribution of diameters was tested for normality using the Shapiro-Wilk test (17). Pearson's correlation coefficient (r) and Spearman's rank correlation

coefficient (ρ) were computed for the paired ultrasound and gross pathology diameter estimates. $P < 0.05$ from a t test (for r) or sign test (for ρ) was considered evidence of statistically significant correlation. Agreement of the gross pathology and ultrasound diameter measurements was also assessed using the graphical method of Bland and Altman (18). In this analysis, the ultrasound diameter estimate was subtracted from the gross pathology estimate, and the difference was plotted against the mean of the two measurements. The mean and SD of the measurement difference were computed for comparison with the estimated diameters.

Determination of tumor growth curves as functions of tumor diameter. Tumors that remained small enough to fit within the 12×12 mm^2 two-dimensional field of view of the ultrasound system in at least three imaging sessions were selected for diameter growth curve analysis. The maximum sagittal diameters of these tumors were measured in ultrasound images using the three-dimensional analysis software. For each tumor, the measured diameters were plotted as functions of time elapsed since initial detection, separate exponential diameter growth curves were fit by linear regression of the logarithm of the diameter data, and diameter doubling times were estimated from the fitted curves. Agreement between the experimental data and the fitted exponentials was assessed by computing coefficients of determination (r^2) for the fitted curves.

Determination of tumor growth curves as functions of tumor volume. Volume growth curves were also constructed for tumors that were entirely contained by the $12 \times 12 \times 9$ mm^3 three-dimensional ultrasound field of view in at least three imaging sessions. Tumor volumes were determined by manual image segmentation (16). In this procedure, tumor boundaries were manually outlined in parallel slices separated by 50 μm in the three-dimensional ultrasound images. The areas of the outlined contours were summed and multiplied by the interslice distance to compute tumor volume. As in the analysis of the diameter data, exponential volume growth curves were fit by linear regression, coefficients of determination were computed to assess the goodness of fit of the exponential function, and volume doubling times were estimated from the exponential curve fits.

Results

Summary of three-dimensional ultrasound imaging experiments. Forty-five transgenic PSP-TGMAP mice were imaged a total of 278 times. Tumor incidence and ultrasound tumor detection results for all 45 mice are summarized in Table 1. A total of 18 tumors were identified by ultrasound imaging and confirmed by gross pathology and histopathology in 14 different mice between ages 4 and 8 months, including 12 ventral prostate tumors, 4 dorsolateral prostate tumors, and 3 anterior prostate tumors. Nineteen mice without macroscopic tumors (but usually with microscopic prostate cancer foci; see Materials and Methods) that were either sacrificed or died while under anesthetic were also included in the detection study. As discussed below in the longitudinal imaging results, partway through the experiment the imaging protocol was changed from biweekly to weekly ultrasound examinations. As a result of this modification, 12 of the original 45 mice were removed from the detection study to maintain a manageable imaging workload. Two of the removed mice developed palpable tumors in a period when the time elapsed since their most recent ultrasound examination exceeded 14 days. The remaining 10 removed mice survived beyond 8 months when the imaging study ended. Two of those mice developed palpable tumors after the end of imaging (one at 10 months and the other at 11 months), and the other eight mice were euthanized at 11 months and had no macroscopic tumors.

Correspondence of three-dimensional ultrasound imaging with three-dimensional reconstructed serial histology slides. Three-dimensional ultrasound images were compared with serial

histology sections to show the fidelity of the ultrasound images of PSP94-TGMAP tumors. Figures 1 and 2 show representative two-dimensional ultrasound images and corresponding histology slides from the 7.3 mm diameter ventral prostate tumor. Figure 1*A* shows three orthogonal planes through a three-dimensional ultrasound image of the tumor. The Supplementary Fig. S1 available from the electronic edition of the journal includes a movie showing user manipulation of the three-dimensional ultrasound image using the image reconstruction software. In the movie, the user slices and rotates the three-dimensional image in dynamic cube view format to reveal the tumor border outlined during image segmentation; then, the tumor surface is displayed and rotated in the orthogonal plane view shown in Fig. 1*A*. Figure 1*B* shows orthogonal planes through a three-dimensional reconstruction of 70 H&E-stained serial histology slides obtained from the same tumor. The visualization software allows the user to enlarge the histology data up to the $\times 10$ magnifications used during digitization and to rotate and slice through the volume in the manner shown in the ultrasound movie, so histologic details of the specimen can be inspected in three dimensions. A movie showing a sequence of orthogonal plane views of the three-dimensional histology reconstruction is available online (Supplementary Fig. S2). Figure 1*C* shows a transverse two-dimensional ultrasound image of this ventral prostate tumor, and Fig. 1*D* shows the corresponding high-magnification histology slide.

Figure 2 shows a series of two-dimensional ultrasound images extracted from the three-dimensional image of the same ventral prostate tumor along with corresponding serial histology slides running from the caudal end of the tumor to the cranial end. The relative locations of the bladder, seminal vesicles, and other

Table 1. Macroscopic tumor incidence in all mice in the study population

	Ultrasound diagnosis			No. mice
	Positive	Negative	No decision	
Included mice				
Macroscopic cancer present	13	1	0	14
Macroscopic cancer absent	0	19	0	19
Subtotal	13	20	0	33
Sensitivity (%)		95		
Specificity (%)		100		
Removed mice				
Macroscopic cancer present	0	0	4	4
Macroscopic cancer absent	0	0	8	8
Subtotal	0	0	12	12
Total	13	20	12	45

NOTE: The set of included mice consists of all subjects for which prospective diagnoses were made by the ultrasound operators on the same date the animals were euthanized for pathology. Twelve mice were removed from the detection study to maintain a manageable imaging workload when the protocol was changed from biweekly to weekly ultrasound examinations.
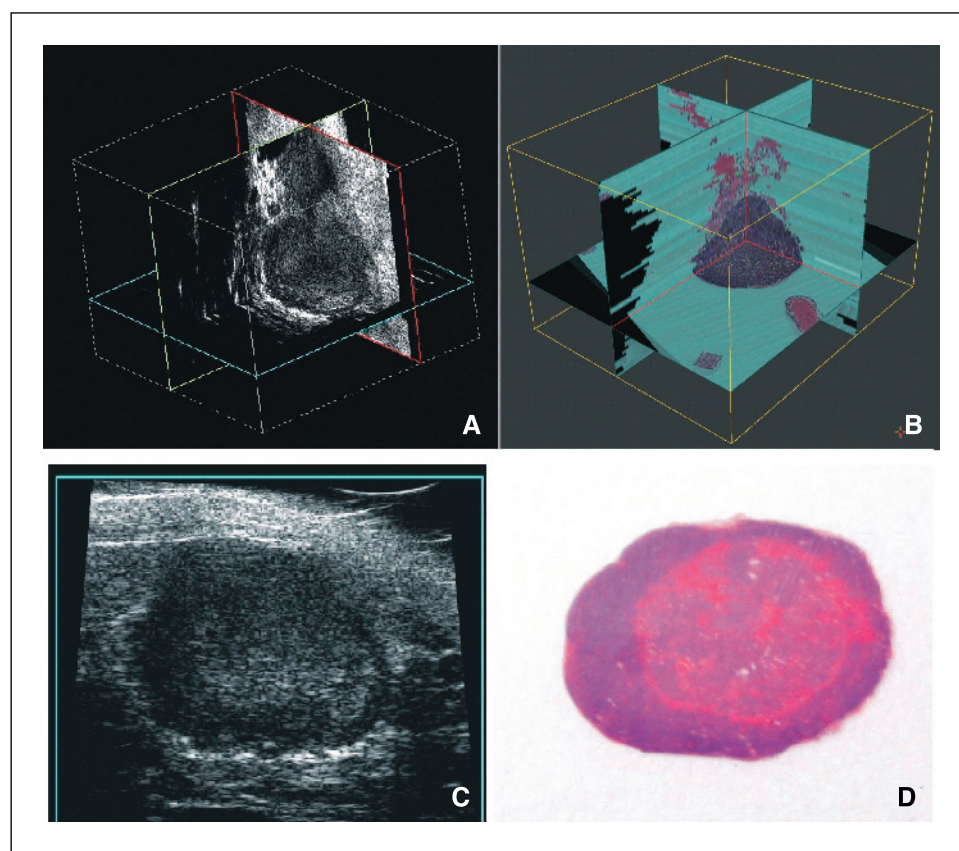
Figure 1. Three-dimensional ultrasound image of a genetically engineered mouse prostate cancer tumor confirmed by three-dimensionally reconstructed serial histology slides. *A,* three-dimensional image of a ventral prostate tumor mass displayed using three orthogonal planes through the ultrasound image volume. A movie showing user manipulation of the three-dimensional ultrasound image is available as Supplementary Data from the Journal Web site. *B,* orthogonal planes through a three-dimensional reconstruction of the serial H&E-stained histology slides from the same tumor. *C,* transverse two-dimensional ultrasound image of the same ventral prostate tumor. The tumor appears as a hypoechoic border surrounding a brighter central core with heterogeneous image texture. *D,* corresponding two-dimensional histology slide. H&E staining, ×4.

periprostatic tissues usually differ in the ultrasound and histology images because those structures tend to move when the abdominal wall is opened during dissection.

Figures 1 and 2 illustrate several characteristics of the PSP-TGMAP tumor model that can be observed using three-dimensional ultrasound imaging. First, the size and shape of the tumor can be determined by slicing through the image volume. Second, each of the slices taken from this tumor show a hypoechoic ring (i.e., the outer tumor area scatters ultrasound weakly and therefore appears dark in the images) surrounding a central region of heterogeneous image texture. High-magnification histologic examination indicates that the outer hypoechoic area consisted of a high density of sheets of poorly differentiated prostate cancer cells, including small cell carcinoma, with few blood vessels. The high-power view of the H&E-stained slides also reveals that the central core, where the tumor appears brighter in the ultrasound images, contains a lower density of poorly differentiated prostate cancer cells surrounded by vascular and hemorrhaged regions (a similar structure is shown in Fig. 3D). The histology slides show that the peripheral dark ring and the brighter central area are separated by a thin layer of ill-defined fibrous stroma tissues. The appearance of a hypoechoic outer ring appears to be the primary factor that allows these murine prostate tumors to be detected in ultrasound images. Third, the seminal vesicles and vas deferens are recognizable in the ultrasound images as those structures come into view in Fig. 2. Although these male accessory glands are also hypoechoic, they can be distinguished from the prostate tumor by considering the size and shape of each structure in the three-dimensional images. Finally, as illustrated in Fig. 2, there is little or no contrast between normal prostate and surrounding healthy tissues in the ultrasound images, so normal

prostate tissue is unlikely to be misclassified as cancerous by ultrasound imaging.

Longitudinal imaging of tumor progression and measurement of growth curves. Four tumors yielded sufficient images for longitudinal analysis, meaning images were acquired on at least three different days where the maximum diameter of the tumor fit within the 12×12 mm^2 two-dimensional field of view of the ultrasound system. Longitudinal measurements were challenging with the PSP-TGMAP model because macroscopic prostate tumors appear at different, and hence unpredictable, ages in different mice and progress very rapidly once they begin to develop. Under the original protocol, mice were imaged every 2 weeks after reaching age 4 months to screen for tumor development. However, the initial results indicated that the tumors could grow from sizes undetectable by ultrasound to over 10 mm in diameter within 14 days, so the protocol was changed to require weekly screening examinations to ensure more lesions would be imaged while still relatively small. Once a lesion was detected, that mouse was imaged every 2 to 3 days to monitor tumor growth. Mice were euthanized when the tumor burden shown by ultrasound became large or the animal's health deteriorated. Animals were imaged and euthanized on the same day to enable comparisons of ultrasound and pathology observations.

Figure 3A shows a representative longitudinal series of two-dimensional slices from nine different three-dimensional ultrasound images of a mouse that developed a large ventral prostate tumor. The mouse was 30 weeks of age on the date, designated day 0, on which the ultrasound image shown in the first panel yielded a measured sagittal tumor diameter of 5.33 mm. The ventral prostate tumor grew rapidly to 5.52, 6.30, 6.71, 8.32, 8.79, 9.86, 10.05, and

10.53 mm diameter on days 1, 4, 5, 10, 12, 14, 15, and 18, respectively. Figure 3*B* presents the gross pathology specimen that was resected on day 18. The H&E-stained photomicrographs shown at ×4 magnification in Fig. 3*C* and at ×25 magnification in Fig. 3*D* show extensive invasive prostate cancer characterized by a poorly differentiated, high-volume neoplasm. The prostate cancer is predominantly hypoechoic and appears dark in the images with some medium echogenicity in the center. Most of the tumor appears sharply outlined with some rough and heterogeneous areas relative to the more echogenic periprostate fibrofatty tissue (Fig. 3*C* and *D*).

Examples of tumors observed in additional mice are presented in Fig. 4*A* to *D*. Figure 4*A* shows a transverse slice through a three-dimensional ultrasound image of a mouse with two ventral prostate tumors and one dorsolateral prostate tumor accompanied by the resected gross specimen and corresponding transverse histology slide at low power (×4) and high power (×25). A movie showing a three-dimensional ultrasound image of these tumors in dynamic cube view format is available online (Supplementary Fig. S3). Figure 4*B* shows an anterior prostate tumor with gross and histopathology.

Mice were not regularly screened for metastatic tumors using ultrasound, but two examples are presented to show the feasibility of imaging metastases in these transgenic mice. One large lymph node metastasis was identified near the prostate of one mouse.

Figure 4*C* shows a transverse slice through the three-dimensional ultrasound image of this lymph node metastasis, the corresponding gross pathology specimen, and H&E-stained photomicrographs of a transverse section through the tumor at low power (×4) and high power (×25). The relatively bright central region of the metastasis in the ultrasound image appears to correspond to a large central necrotic region ∼5 mm in diameter shown in the histology slides (Fig. 4*C*, H&E, ×4 and ×25). Figure 4*D* shows a transverse plane from a three-dimensional ultrasound image of the left lobe of the liver of another mouse with highly advanced prostate cancer. The focal thickening of the liver indicates the presence of a metastasis. A photograph of the under surface of the left lobe (Fig. 4*D*, gross pathology) shows the metastasis, and histopathology (Fig. 4*D*, H&E) confirmed the lesion was malignant.

Figure 5*A* shows exponential growth curves that were fit to maximum sagittal diameter measurements in longitudinal ultrasound images of four different tumors. The coefficients of determination for the four growth curves (r^2 = 0.943, 0.980, 0.996, and 0.988) indicate that an exponential function realistically models diameter growth during the period of rapid tumor progression in this model. Diameter doubling times estimated from the exponential curve fits were 10.3, 15.7, 18.7, and 42.8 days for these tumors.

To confirm the diameter growth curves, longitudinal volume measurements were also obtained from two of these tumors that fit

Figure 2. Comparison of cross-sectional planes extracted from a three-dimensional ultrasound image with serial histology slides. The 12 serial transverse planes are from a three-dimensional ultrasound image volume acquired the same day the mouse was euthanized. The 12 histology slides were selected from a larger set obtained at ∼50 μm spacing. The prostate and the other male accessory glands are labeled with *arrows*.

▷ =prostate cancer
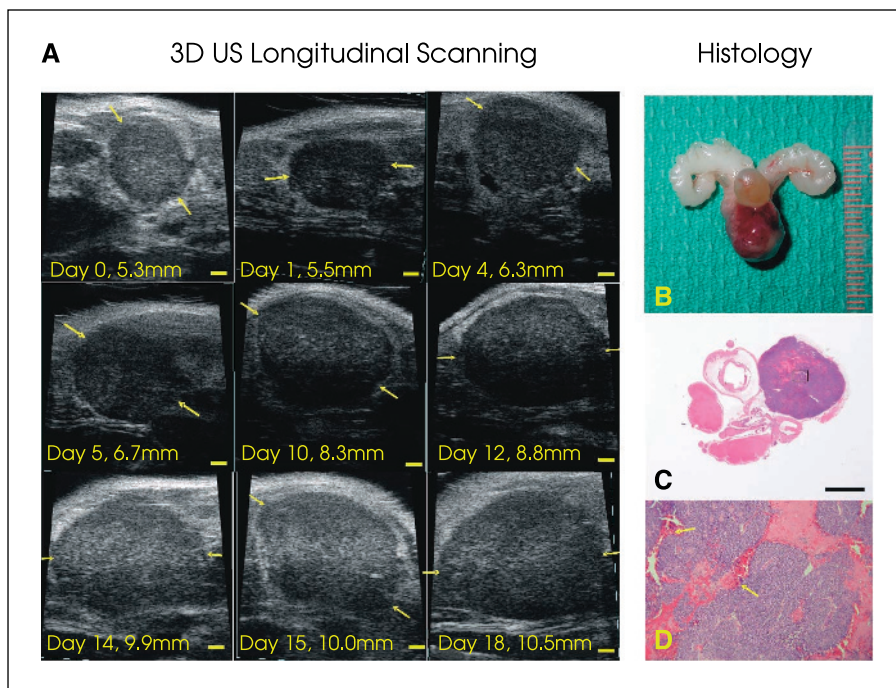▶ =Seminal vesicle
▶ =Vas deferens
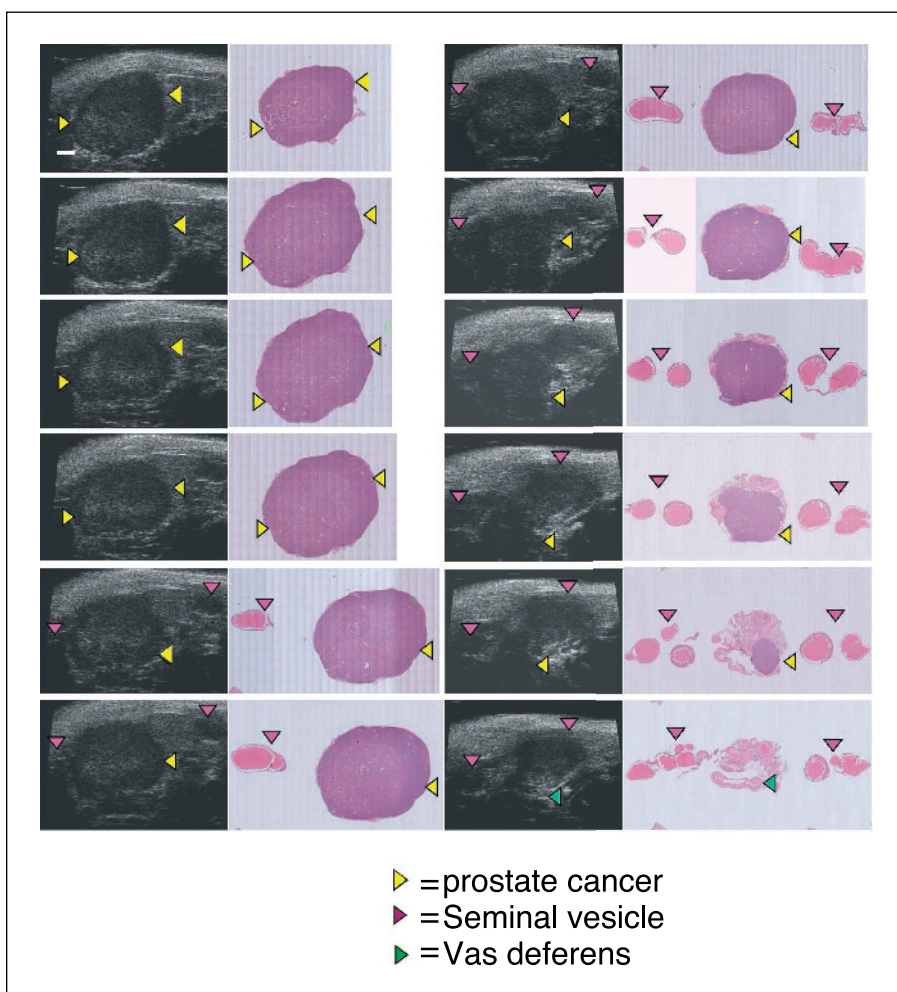
Figure 3. Longitudinal and cross-sectional ultrasound images of prostate tumors with gross pathology and histopathology confirmation. *A,* transverse ultrasound images of the same ventral prostate tumor (*arrows*) acquired on 9 different days within an 18-day period. The ventral surface of the abdominal wall is shown at the *top* of the images and the deeper abdominal and retroperitoneal structures are at the *bottom* of the images. *B,* gross pathology specimen of the same tumor obtained on the same day as the ultrasound image shown in day 18. *C* and *D,* low-power (×4) and high-power (×25) photomicrographs of transverse plane H&E-stained histology slides of the same tumor showing extensive invasion of the prostate by a high-grade, high-volume neoplasm.

within the $12 \times 12 \times 9$ mm^3 image volume on at least 3 separate days. The measured tumor volumes are plotted against elapsed time in Fig. 5*B*. Exponential functions also fit the volume data well, yielding coefficients of determination of $r^2 = 0.939$ and 0.986. Volume doubling times estimated from the exponential curve fits were 4.9 and 12.9 days.

Agreement of ultrasound and gross pathology diameter measurements. Paired sagittal diameter measurements obtained from three-dimensional ultrasound images and gross pathology specimens of 11 tumors in the mice that were diagnosed tumor positive by the ultrasound operators are plotted in Fig. 5*C*. The plot shows a straight-line fit to the data obtained by linear regression. The diameter data were normally distributed as assessed using the Shapiro-Wilk test ($W = 0.880$ and $P = 0.104$). Pearson's and Spearman's correlation coefficients were $r = 0.998$ and $\rho = 1.000$, respectively, and indicated significant ($P < 0.001$) correlation between the ultrasound and gross pathology diameter measurements. The Bland-Altman scatter plot (Fig. 5*D*) shows the close agreement of the two methods of measurement. The mean difference between the ultrasound and gross pathology measurements was ~0, and the SD of the difference (0.30 mm) was small compared with the diameters of the tumors.
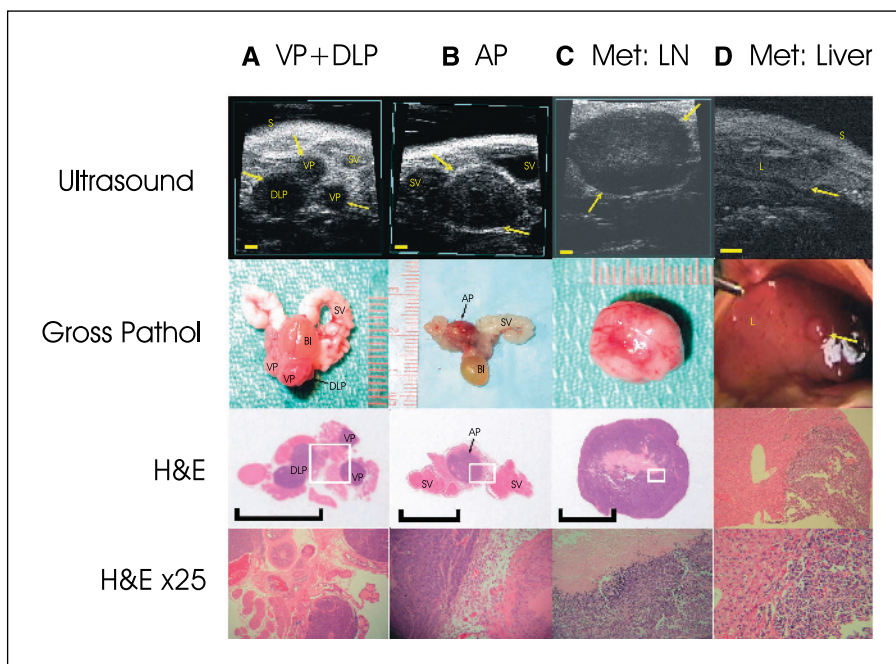

Figure 4. Cross-sectional ultrasound images and gross pathology and histopathology confirmation of prostate tumors in different lobes and metastatic locations. *A,* transverse ultrasound image of a mouse with two ventral prostate (*VP*) tumors and one dorsolateral prostate (*DLP*) tumor (*arrows*) with corresponding gross pathology specimen and low-power (×4) and high-power (×25) transverse H&E-stained histology slides. *Bl,* bladder; *S,* skin and s.c. tissue; *SV,* seminal vesicle. *B,* transverse ultrasound image of an anterior prostate (*AP*) tumor (*arrows*) with corresponding gross pathology specimen and low-power and high-power transverse H&E-stained histology slides. *C,* transverse ultrasound image of a lymph node metastasis (*Met: LN; arrows*) with corresponding gross pathology specimen and low-power and high-power transverse H&E-stained histology slides. *D,* transverse ultrasound image of a left lobe of a liver (*L*) showing a focal thickening (*Met: Liver; arrow*) produced by a metastatic tumor and corresponding gross pathology specimen and low-power and high-power transverse H&E-stained histology slides. *Bar,* 1 mm (all ultrasound images) and 5 mm (all histology slides).
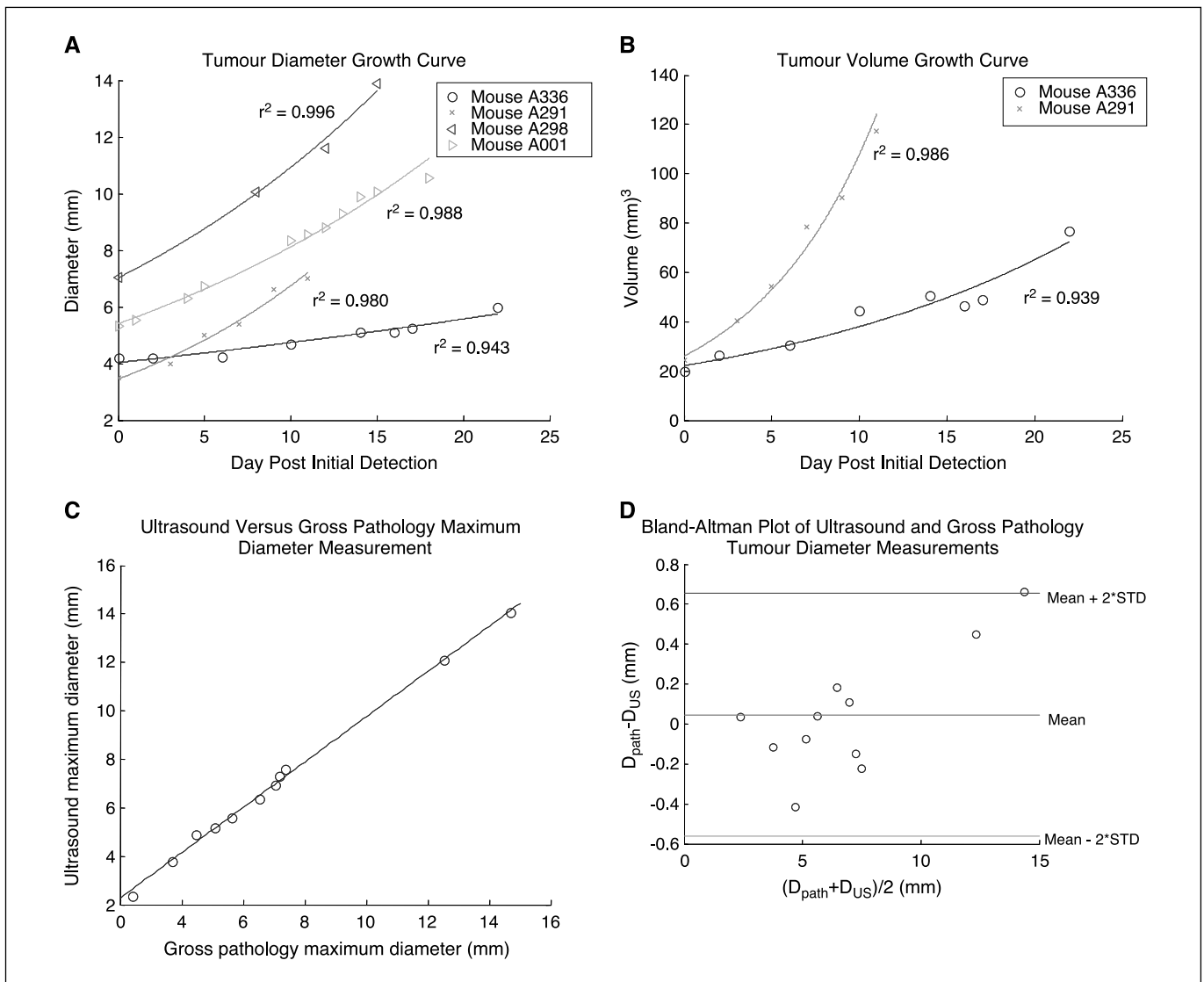
Figure 5. Tumor size measurements obtained from ultrasound imaging and gross pathology. *A,* maximum sagittal diameters of four prostate tumors measured in two-dimensional ultrasound images with fitted exponential growth curves. *B,* volumes of two prostate tumors measured in three-dimensional ultrasound images with fitted exponential growth curves. *C,* correlation of 11 maximum sagittal tumor diameters measured by ultrasound imaging and gross pathology assessed by linear regression ($r = 0.998$; $P < 0.001$). *D,* Bland-Altman (16) graphical analysis of agreement of the 11 pairs of tumor diameter measurements plotted in (*C*). The difference between the diameter estimated by gross pathology (D_{path}) and the diameter estimated using ultrasound (D_{US}) is plotted against the average of the two measurements.

Ultrasound tumor detection sensitivity and specificity. Prospective diagnoses were made by the ultrasound operators for 33 mice, including 14 with prostate tumors subsequently confirmed by pathology and 19 without tumors (Table 1). The 2.4 mm diameter ventral prostate lesion shown in Fig. 4*A* was the smallest tumor detected by the operators (the ventral prostate tumor appears smaller than 2.4 mm in Fig. 4*A* because the image plane shown does not contain the maximum diameter of the ventral prostate tumor). The ultrasound operators' tumor detection sensitivity and specificity were 95% and 100%, respectively.

Discussion

The ability to noninvasively quantify tumor burden *in vivo* in genetically engineered mouse models will ultimately lead to the development of more accurate models of human cancer that are better suited for evaluating and optimizing preclinical cancer therapy. The objectives of cancer imaging in small animal models include limiting the statistical variability of preclinical studies by following specific tumors through the course of disease, reducing the number of mice required for a study, and maximizing the amount of data obtained from each mouse. *In vivo* imaging provides data that are not available postmortem, such as growth curves that quantify the kinetics of tumor progression and treatment responses.

Small animal cancer imaging may be done with instruments equivalent to any of the prominent clinical diagnostic imaging technologies, including X-ray computed tomography (CT), MRI, positron emission tomography, single photon emission CT, and ultrasound as well as several emerging optical techniques (5). As reviewed in ref. 6, each of these technologies offers different combinations of advantages and disadvantages. Ideally, a small animal cancer imaging technology should be sensitive to tumors in specific models, produce images with high spatial resolution for

detecting and measuring the sizes of small early-stage tumors, acquire those images rapidly, and employ equipment that is economical to purchase, operate, and maintain. Furthermore, when longitudinal studies are required, the imaging examination should be as harmless to the animal as possible so imaging may be done as frequently as necessary without introducing the risk that the radiation employed for imaging affects the progression of cancer in the animal model.

Three-dimensional ultrasound microimaging provides an attractive combination of the characteristics required of a small animal cancer imaging technology. The strengths and weaknesses of ultrasound for microimaging are similar to its advantages and disadvantages for clinical diagnostic imaging (19). Ultrasound is nonionizing and provides good soft tissue contrast and high spatial resolution (e.g., ~100 μm using the 30 MHz transducer employed in this study) without the need for i.v. contrast agents. The real-time (up to 32 two-dimensional frames per second with the Vevo 660 system) frame rate of ultrasound combined with the use of a handheld transducer probe permits an ultrasonographer to rapidly survey an organ for lesions, thereby improving the efficiency of multiple-animal longitudinal studies. Ultrasound instruments are portable and economical, so scanners are easily incorporated into animal surgery or barrier housing facilities (20).

Challenges in using ultrasound include smaller penetration depth and field of view than X-ray CT or MRI, an inability to image bony or air-filled anatomy, and operator-dependent image quality. As is the case for clinical ultrasound, penetration depth is limited by frequency-dependent attenuation of the ultrasound pulse, so ultrasound systems for small animal imaging do not produce whole-body cross-sectional images as are provided by X-ray CT and MRI. However, it is noteworthy that the $12 \times 12 \times 9$ mm^3 field of view used in this study was chosen to improve visualization of small tumors and is not the largest field of view available from the ultrasound system, which is currently $20 \times 20 \times 15$ mm^3. Furthermore, the three-dimensional imaging technology described in this article helps alleviate operator dependence of image quality and reduces the variability of volume measurements compared with two-dimensional ultrasound (16).

This article describes the first use of three-dimensional ultrasound microimaging to monitor tumor progression in a transgenic mouse cancer model. The study specifically employed a *PSP94* gene-directed transgenic prostate cancer model with characteristics similar to the TRAMP model that is internationally used for preclinical trials of prostate cancer therapies. Just as different types of clinical cancers have different ultrasound characteristics, the observations made in this study are specific to the PSP94 model but can be considered indicative of the categories of anatomic and growth information that can be expected from ultrasound imaging of mouse cancer models. The stochastic appearance of macroscopic prostate cancer masses in a transgenic model, such as the PSP-TGMAP, is characterized by rapid tumor progression to late-stage cancer in ~14 days, with the tumors becoming palpable near the end of the rapid-growth period. Fast-growing tumor models should enable efficient preclinical trials, but the late-stage, palpable prostate tumors are usually unresponsive to hormone therapy and therefore possess little value for treatment evaluation. The design of a longitudinal treatment study must ensure that the number of animals used permits each animal to be imaged frequently relative to the growth rate of the tumors. This constraint implies that the investigator must have approximate knowledge of the tumor growth rate before the study; otherwise, the study population may need to be reduced while a trial is in progress as occurred in this article.

Our results show that three-dimensional ultrasound imaging detects macroscopic prostate tumors with up to 100% sensitivity in the period of rapid exponential growth, when the masses are too small to be palpable and may still be suitable for use in evaluation of antitumor treatments. Furthermore, longitudinal ultrasound imaging allow prostate tumor progression to be measured during the exponential growth period and therefore should also enable changes in growth rates to be measured in treatment studies. Three-dimensional ultrasound imaging can determine tumor doubling time over a wide range of growth rates as observed in four of the mice in the current study (Fig. 5*A* and *B*). This observation suggests that the use of three-dimensional ultrasound does not impose a significant limitation on the range of tumor growth rates used in a study. This result also indicates that the progression of prostate cancer in our model shows a certain degree of heterogeneity, as does clinical cancer and other mouse models, such as the TRAMP model. The wide range of growth rates observed in these tumors underscores the necessity of performing volume and growth rate measurements for individual tumors, which are only possible using *in vivo* imaging.

The study showed additional characteristics of three-dimensional ultrasound microimaging that make the technology well suited for preclinical cancer research. The mice tolerate repeated imaging sessions well, which may be attributed to the use of gas rather than injected anesthetic as well as the benign nature of ultrasound exposure. Volumetric data acquisition requires brief imaging examinations lasting ~15 to 30 minutes per animal. In addition, our initial observations suggest that ultrasound image texture can be correlated with cell density in mouse prostate cancer foci, necrotic areas of tumors, and blood vessel distribution in tumors. This research will benefit from recent adaptations of Doppler (21) and contrast-enhanced (22) ultrasound methods for vascular imaging of mouse cancer models. The exact relationship between ultrasound and histology characteristics should be expected to vary at different points in tumor progression and also among different tumor models, but the results presented here indicate that visual comparisons of ultrasound images with H&E-stained histology slides can aid in the interpretation of the ultrasound images. Such comparisons will have to be done independently for each tumor model of interest.

Acknowledgments

References

1. Greenberg NM, Demayo F, Finegold MJ, et al. Prostate cancer in a transgenic mouse. Proc Natl Acad Sci U S A 1995;92:3439–43.
2. Masumori N, Thomas TZ, Chaurand P, et al. A probasin-large T antigen transgenic mouse line develops prostate adenocarcinoma and neuroendocrine carcinoma with metastatic potential. Cancer Res 2001; 61:2239–49.
3. Abate-Shen C, Shen MM. Mouse models of prostate carcinogenesis. Trends Genet 2002;18:S1–5.
4. Huss WJ, Maddison LA, Greenberg NM. Autochthonous mouse models for prostate cancer: past, present and future. Semin Cancer Biol 2001;11:245–60.
5. Therasse P, Arbuck SG, Eisenhauer EA, et al. New guidelines to evaluate the response to treatment in solid tumors. European Organization for Research and Treatment of Cancer, National Cancer Institute of the United States, National Cancer Institute of Canada. J Natl Cancer Inst 2000;92:205–16.
6. Weissleder R. Scaling down imaging: molecular mapping of cancer in mice. Nat Rev Cancer 2002;2:1–8.
7. Hsu CX, Ross BD, Chrisp CE, et al. Longitudinal cohort analysis of lethal prostate cancer progression in transgenic mice. J Urol 1998;160:1500–5.
8. Adams JY, Johnson M, Sato M, et al. Visualization of advanced human prostate cancer lesions in living mice by a targeted gene transfer vector and optical imaging. Nat Med 2002;8:891–7.
9. Lyons SK, Meuwissen R, Krimpenfort P, Berns A. The generation of a conditional reporter that enables bioluminescence imaging of Cre/loxP-dependent tumorigenesis in mice. Cancer Res 2003;63:7042–6.
10. Xie X, Luo Z, Slawin KM, Spencer DM. The EZC-prostate model: noninvasive prostate imaging in living mice. Mol Endocrinol 2004;18:722–32.
11. Turnbull DH, Ramsay JA, Shivji GS, et al. Ultrasound backscatter microscope analysis of mouse melanoma progression. Ultrasound Med Biol 1996;22:845–53.
12. Gabril MY, Onita T, Ji PG, et al. Prostate targeting: PSP94 gene promoter/enhancer region directed prostate tissue-specific expression in a transgenic mouse prostate cancer model. Gene Ther 2002;9:1589–99.
13. Duan WM, Gabril MY, Moussa M, et al. Knock-in of SV40 Tag oncogene in a mouse adenocarcinoma of the prostate (KIMAP) model demonstrates advantageous features over the transgenic model. Oncogene 2005; 24:1510–24.
14. Gabril MY, Duan WM, Wu GJ, et al. A novel knock-in prostate cancer model demonstrates biology similar to that of human prostate cancer and suitable for preclinical studies. Mol Ther 2005;11:348–62.
15. Foster FS, Zhang MY, Zhou YQ, et al. A new ultrasound instrument for *in vivo* microimaging of mice. Ultrasound Med Biol 2002;28:1165–72.
16. Fenster A, Downey DB, Cardinal HN. Three-dimensional ultrasound imaging. Phys Med Biol 2001;46: R67–99.
17. Shapiro SS, Wilk MB. An analysis of variance test for normality (complete samples). Biometrika 1965;52: 591–611.
18. Bland JM, Altman DG. Statistical methods for assessing agreement between two methods of clinical measurement. Lancet 1986;1:307–10.
19. Foster FS, Pavlin CJ, Harasiewicz KA, Christopher DA, Turnbull DH. Advances in ultrasound biomicroscopy. Ultrasound Med Biol 2000;26:1–27.
20. Klaunberg BA, Lizak MJ. Considerations for setting up a small-animal imaging facility. Lab Anim (NY) 2004;33:28–34.
21. Goertz DE, Yu JL, Kerbel RS, Burns PN, Foster FS. High-frequency Doppler ultrasound monitors the effects of antivascular therapy on tumor blood flow. Cancer Res 2002;62:6371–5.
22. Goertz DE, Cherin E, Needles A, et al. High frequency nonlinear B-scan imaging of microbubble contrast agents. IEEE Trans Ultrason Ferroelectr Freq Control 2005;52:65–79.